



# Impact of extracellular matrix and collagen network properties on the cervical intervertebral disc response to physiological loads: A parametric study

Mohamed Amine Chetoui, Dominique Ambard, Patrick Cañadas, Pascal Kouyoumdjian, Pascale Royer, Simon Le Floc'h

## ► To cite this version:

Mohamed Amine Chetoui, Dominique Ambard, Patrick Cañadas, Pascal Kouyoumdjian, Pascale Royer, et al.. Impact of extracellular matrix and collagen network properties on the cervical intervertebral disc response to physiological loads: A parametric study. Medical Engineering & Physics, 2022, 110, pp.103908. 10.1016/j.medengphy.2022.103908 . hal-04048056

**HAL Id: hal-04048056**

**<https://hal.science/hal-04048056v1>**

Submitted on 29 Mar 2023

**HAL** is a multi-disciplinary open access archive for the deposit and dissemination of scientific research documents, whether they are published or not. The documents may come from teaching and research institutions in France or abroad, or from public or private research centers.

L'archive ouverte pluridisciplinaire **HAL**, est destinée au dépôt et à la diffusion de documents scientifiques de niveau recherche, publiés ou non, émanant des établissements d'enseignement et de recherche français ou étrangers, des laboratoires publics ou privés.



Distributed under a Creative Commons Attribution - NonCommercial - NoDerivatives 4.0 International License

# Impact of extracellular matrix and collagen network properties on the cervical intervertebral disc response to physiological loads: A parametric study

Mohamed Amine Chetoui<sup>a,\*</sup>, Dominique Ambard<sup>b</sup>, Patrick Canãdas<sup>b</sup>, Pascal Kouyoumdjian<sup>c</sup>, Pascale Royer<sup>b</sup>, Simon Le Floc'h<sup>b</sup>

<sup>a</sup>*Pascal Institute UMR6602, Univ. of Clermont Auvergne, Aubière, France*

<sup>b</sup>*LMGC UMR5508, Univ. of Montpellier, CNRS, Montpellier, France*

<sup>c</sup>*Orthopedic surgery and trauma service, Spine surgery, CHRU of Nîmes, Nîmes, France*

---

## Abstract

Current intervertebral disc finite element models are hard to validate since they describe multi-physical phenomena and contain a huge number of material properties. This work aims to simplify numerical validation/identification studies by prioritizing the sensitivity of intervertebral disc behavior to mechanical properties. A 3D fiber-reinforced hyperelastic model of a C6-C7 intervertebral disc is used to carry out the parametric study. 10 parameters describing the extracellular matrix and the collagen network behaviors are included in the parametric study. The influence of varying these parameters on the disc response is estimated during physiological movements of the head, including compression, lateral bending, flexion, and axial rotation. The obtained results highlight the high sensitivity of the disc behavior to the stiffness of the annulus fibrosus extracellular matrix for all the studied loads with a relative increase in the disc apparent stiffness by 67% for compression and by 57% for axial rotation when the annulus stiffness increases from 0.4 to 2 MPa. It is also shown that varying collagen network orientation, stiffness, and stiffening in the studied configuration range have a noticeable effect on rotational motions with a relative apparent stiffness difference reaching 6.8%, 10%, and 22%, respectively, in lateral bending. However, the collagen orientation does

---

\*Corresponding author

Email address: mohamed-amine.chetoui@centrale-marseille.fr (Mohamed Amine Chetoui)

not affect disc response to axial load.

*Keywords:* Intervertebral disc, FE analysis, Fibrous soft tissue, Porous media, Cervical spine kinematics.

---

## 1. Introduction

Tissue engineering, replacement and regeneration techniques are increasingly used in the treatment of intervertebral disc diseases. While synthetic material replacements are still limited by the biocompatibility hurdle, biomaterials designed for annulus fibrosus (AF) and nucleus pulposus (NP) repair and replacement have managed to mimic IVD biology and have shown promising results [1, 2]. However, without focusing on mechanical compatibility, these biomaterials-based solutions have not yet shown a long-term performance [2, 3]. Mechanical compatibility is not less critical than biocompatibility since it permits to restore biomechanical behavior of the motion segment, and thus reduces re-herniation and promotes longevity [2, 4]. Therefore, a sophisticated comprehension of the biomechanical behavior of the intervertebral disc is invaluable to enhancing the performance of biomaterial-based techniques.

The intervertebral disc (IVD) biomechanical behavior is complex and it can not be explored using only experiments or analytical methods [5]. Spine and disc biomechanics are commonly studied using finite element (FE) analysis. FE models developed for the IVD are increasingly improved. However, they become more difficult to implement and validate.

Recent models take into account complex structural phenomena taking part in this soft tissue such as the osmotic role of proteoglycans and the mechanical contribution of collagen fibers including fiber cross-links, fiber/matrix interaction, and interlamellar behavior (e.g. [6, 7, 8, 9]). These models generally managed to provide a good agreement with experimentation. However, the uniqueness of the identified mechanical properties is not guaranteed given their relatively large number and their possible interdependency [10, 11]. Furthermore, the

22 impact of the experimentation-related uncertainties on the identification studies remains sig-  
23 nificant and it is reflected in the large scatter of the IVD mechanical properties values. Most  
24 of the biomechanical experimental tests used in the parameter identification are performed  
25 ex-vivo. Cadaveric tissue, generally used to perform biomechanical ex-vivo experimental tests,  
26 undergoes several changes in properties related to the conservation conditions which leads to  
27 variability in the experimental data [12]. In addition, the relevance of each parameter de-  
28 pends on the load type and the nature of the experimental data used for the identification.  
29 For example, the micro-channels configuration of a porous medium may increase the apparent  
30 stiffness of the tissue in the case of confined consolidation compared to the unconfined one  
31 [13].

32 Computational validation issues could be treated by several approaches. Multi-objective  
33 optimization and the use of huge experimental databases could be suggested. However, these  
34 solutions tend to complicate the studies and raise their time-memory cost. Different ap-  
35 proaches, based upon the exploitation of quantitative MRI for the construction and the val-  
36 idation of FE models were introduced [14, 11]. This technique seems efficient but is limited  
37 by the MRI resolution and needs to be clinically validated. Recent studies introduced prob-  
38 abilistic and deterministic deep learning approaches to reduce the cost of complex behavior  
39 tissue models including porous media, hyperelastic anisotropic tissue, and multiscale models.  
40 Despite their promising results in model reduction and simulation acceleration, these meth-  
41 ods present some limitations related to the handle with irregular mesh and some particular  
42 boundary conditions [15, 16, 17]. Therefore, sensitivity studies remain an essential tool to  
43 improve and validate IVD FE models [18, 5]. Studying the impact of varying the parameter  
44 values permits to better understand the IVD model biomechanics and manage the validation  
45 studies. It allows sorting parameters by relevance and fixing the values of those with no  
46 significant effect, simplifying the study by focusing on the most important parameters and

47 therefore helping to obtain a more accurate result.

48 Several sensitivity analyses have been conducted on lumbar spine FE models. The impact  
49 of structural, mechanical, and morphological properties of vertebrae, IVD, and ligaments in  
50 the lumbar spine was studied under different loads [19, 20, 21, 22, 5]. The obtained results  
51 have contributed to the understanding of lumbar spine biomechanics and the studying of some  
52 FE models accuracy. However, fewer sensitivity studies have been carried out for the cervical  
53 spine and they are limited on the sensitivity of the stiffness of the spinal components, assumed  
54 to be linear elastic, on spine biomechanics [23, 24]. The current study represents a sensitivity  
55 analysis of C6-C7 IVD mechanical properties using a nonlinear poroelastic FE model with  
56 fiber reinforcement. The objective is to determine and analyze the sensitivity of the model  
57 to both the matrix mechanical properties and the collagen network configuration. For this  
58 purpose, physiological loads are used in the simulations. By prioritizing the contribution of  
59 the model properties in the IVD biomechanics for different load types, this work aims to  
60 create a benchmark for numerical studies.

61

## 62 **2. Material and methods**

### 63 *2.1. Constitutive formulation*

64 The definition of quantities of interest permits to perform the mesh sensibility test and  
65 to choose the constitutive model of the study [25]. In our case, we were interested in the  
66 maximum stress linked to the solid phase, the fluid flow linked to the fluid phase and the  
67 apparent stiffness which is a global quantity linked to the entire domain.

68 The choice of the constitutive model has been based on the quantities of interest and on  
69 the mechanical aspects studied in the literature. In vivo measurements have shown that  
70 the cervical IVD undergoes large strain during physiological motion [26]. It was also shown

71 that the collagen fibers do not contribute only to the tissue response to mechanical loads  
72 but also to its swelling behavior [27, 28]. On the other hand, The compressibility of the  
73 extracellular matrix (ECM) has been largely investigated and discussed. Although several  
74 finite element studies have adopted a nearly-incompressible model for the extracellular matrix,  
75 recent experimental studies have highlighted the auxetic compressible behavior of the annulus  
76 fibrosus [29, 30]. These results revealed the importance of studying the IVD behavior in  
77 large deformation, taking into account the annulus anisotropy, the compressibility of the  
78 extracellular matrix (ECM), and the fluid flow in the porous network.

79 The constitutive formulation implemented for this study is based on the biphasic swelling  
80 model [31, 32, 33]. The IVD is assimilated to a superposition of two immiscible and isothermal  
81 phases: a porous solid skeleton describing the fiber-reinforced extracellular matrix saturated  
82 by an intrinsically incompressible fluid. The total Cauchy stress  $\boldsymbol{\sigma}$  is the summation of the  
83 solid effective stress tensor  $\boldsymbol{\sigma}^e$  and the interstitial fluid stress derived from the hydrostatic  
84 pressure  $p$  and the osmotic pressure  $\Delta\pi$ :

$$\boldsymbol{\sigma} = \boldsymbol{\sigma}^e - (p + \Delta\pi)\mathbf{1} \quad (1)$$

85 The hydrostatic pressure  $p$  is determined by Darcy and mass conservation laws while  
86 respecting the intrinsic incompressibility assumption. The permeability  $k$  of the medium is  
87 taken isotropic and strain-dependent as proposed in [34]. The osmotic pressure  $\Delta\pi$  of the  
88 IVD is expressed in terms of the fixed charge density of the proteoglycans  $C_{fc}$  which is also  
89 taken strain-dependent [33].

$$\Delta\pi = RT(\varphi_i\sqrt{C_{fc}^2 + 4C_e^2} - 2\varphi_e C_e) \quad (2)$$

$$C_{fc} = C_{fc0} \frac{\phi_0}{\phi_0 - 1 + J} \quad (3)$$

where  $\phi_0$  is the initial porosity,  $J$  is the deformation gradient determinant,  $C_{fc}$  and  $C_{fc0}$  are the current and the initial fixed charge densities respectively,  $C_e$  the external salt concentration,  $R$  the universal gas constant,  $T$  the absolute temperature, and  $\varphi_i$  and  $\varphi_e$  respectively the internal and the external osmotic coefficients. The extracellular matrix of the medium is defined by its total strain energy density  $W$ .  $W$  was composed of a compressible Neo-Hookean isotropic part  $W_{NH}$  for the non-fibrillar matrix and an anisotropic part  $W_{fi}$  describing the contribution of each family of fibers  $i$ :

$$W = W_{NH}(\mathbf{C}) + \sum_i W_{fi}(\mathbf{C}, \vec{e}_i) \quad (4)$$

$$W_{NH} = \frac{\mu}{2} (I_1 - 3) - \mu \ln(J) + \frac{\lambda}{2} (\ln(J))^2 \quad (5)$$

90 where  $\mathbf{C}$  is the right Cauchy-Green strain tensor,  $I_1$  is its first invariant and  $\mu$  and  $\lambda$  are  
 91 the parameters of Lamé. The vector  $\vec{e}_i$  represents the director vector of the fiber family  $i$   
 92 orientation. The anisotropic part was taken null in the NP and the CEP. Two families of  
 93 fibers oriented by  $\pm\alpha$  were considered in the AF. The fiber strain energy density of the  $i^{th}$   
 94 fibers population ( $i=1,2$ ) was defined according to [35].

$$W_{fi} = \frac{a_i}{2b_i} \left( e^{b_i[(1-3K)I_{fi}+KI_1-1]^2} - 1 \right) \quad (6)$$

where  $a_i$  (MPa) and  $b_i$  (unitless) are the fiber rigidity and non linearity coefficient,  $K$  is their dispersion and  $I_{fi}$  is a fiber direction invariant written as

$$I_{fi} = \mathbf{C} : (\vec{e}_i \otimes \vec{e}_i) \quad (7)$$

95 The same mechanical parameters were taken for both families of fibers:  $a_i = a_{AF}$  and  
 96  $b_i = b_{AF}$ .

## 97 2.2. Finite element model

98 The unknowns of the equation system were the hydrostatic pressure  $p$  and the three-  
99 component displacement field. We have used Lagrange quadratic (P2) and linear (P1) poly-  
100 nomial functions for the interpolation of the displacement and the pressure, respectively.

101 For this study, we have developed a three-dimensional finite element model of human  
102 C6-C7 IVD. We have constructed a parametric geometry based on six experimental studies  
103 conducted on the cervical spine morphology [36, 37, 38, 39, 40, 41]. The geometry is composed  
104 of a central elliptical *nucleus pulposus* (NP) representing 26% of the total volume, a peripheral  
105 *annulus fibrosus* (AF) surrounding the NP and two cartilaginous endplates (CEP) (Fig. 1).  
106 The geometry was meshed using the software *Gmsh* [42]. A mesh refinement study was per-  
107 formed using 4 20-node hexahedral element meshes with different element number to check  
108 the convergence of our quantities of interest against element size. Local refinement was not  
109 considered given the absence of geometrical irregularities, high-stress gradient, or common  
110 stress concentration areas for the studied loads. The selected mesh has been composed of  
111 5940 hexahedral elements (26106 nodes). The model was implemented in the open-source  
112 software LMGC90 [43].

## 113 2.3. Definition of the fiber orientation

114 The fiber orientation angle  $\alpha$  decreases from the inner to the outer lamella of the AF [44].  
115 To respect this property, we have defined the fiber orientation using local spatial distributions  
116 progressing continuously from the inner to the outer AF. Two parameters were defined,  $\alpha_i$  and  
117  $\alpha_o$ , the fiber angle to the transverse plane, at the inner and at the outer lamella, respectively  
118 (Fig. 2.B). Given the shape of the IVD geometry, it was necessary to define a local coordinate  
119 system centered in the NP center  $O_{NP}$  and satisfying two criteria: i) For each element of  
120 the AF, fibers are defined in lamellae plane, ii) Elements of the same lamella should have



121 the same fiber orientation. At this stage, the shape of the annular mesh has been useful. To  
 122 define this coordinate system we started with the resolution of a thermal problem in which  
 123 we have imposed two different temperatures in the lateral boundary of the AF ( $T_{AF}$ ) and in  
 124 the NP ( $T_{NP}$ ) with  $T_{AF} < T_{NP}$  (Fig. 2.A). The heat flux vector in each node defines its local  
 125 radial vector  $\vec{e}_{r_{AF}}$ . Then, we defined the axial vector  $\vec{e}_{a_{AF}}$  which corresponds to the Z-axis  
 126 of the global coordinate system. The tangential vector  $\vec{e}_{t_{AF}}$  was determined by the cross  
 127 product ( $\vec{e}_{a_{AF}} \wedge \vec{e}_{r_{AF}}$ ). Finally, the vectors  $\vec{e}_1$  and  $\vec{e}_2$  were defined in each node according to  
 128 this relation:

$$\vec{e}_1 = \cos(\alpha) \cdot \vec{e}_{t_{AF}} + \sin(\alpha) \cdot \vec{e}_{a_{AF}} \quad (8)$$

$$\vec{e}_2 = -\cos(\alpha) \cdot \vec{e}_{t_{AF}} + \sin(\alpha) \cdot \vec{e}_{a_{AF}} \quad (9)$$

#### 129 2.4. Model validation

130 A validation process was conducted to find the reference parameter vectors to perform the  
 131 sensitivity study. We have compared the behavior of our model in lateral bending, flexion, and  
 132 axial rotation to experimental previous works by reproducing the applied load described in  
 133 [45, 46, 47]. These experimental studies provide functions describing the C6-C7 IVD rotation  
 134 when it is exposed to a 0 to 2Nm pure moment. To compare the behavior of the current  
 135 model to experimental curves, we have performed 4 tests for each motion by applying 0.5,  
 136 1, 1.5, and 2Nm moments and determined the IVD orientation angle for each test. Then we  
 137 have interpolated these points to find the numerical evolution function of each motion (lateral  
 138 bending, flexion, and axial rotation). The interpolation function used here has been defined  
 139 in the experimental studies and has the following form:  $\theta = \gamma_v + \alpha_v \ln(\beta_v M + 1)$ . where  $\theta$  and  
 140  $M$  are the rotation angle and the applied moment, respectively, and  $\gamma_v$ ,  $\alpha_v$  and  $\beta_v$  are the  
 141 function parameters. In our case, we have taken  $\gamma_v = 0$  for all the loads to start from  $0^\circ$  of

rotation when a null moment is applied. We have manually varied the model parameters to finally find a parameter vector that permits to closely reproduce the experimental behavior of the C6-C7 IVD (Fig. 3). This parameter vector will constitute the reference vector of the parametric study called for the rest of this paper "the basic model". Here, the basic model is not necessarily the best fit combination with a minimized error compared to the experimental curve. However, we are sure that, with the retained combination, the model reproduces the experimental mechanical response used in this validation step.

## 2.5. Boundary conditions for the parametric study

The simulations were performed under uniaxial compression and three physiological independent loads of the cervical spine: lateral bending, axial rotation, and flexion. Each load has been applied in a 3-step sequence (Fig. 4). The first step was a 2-hour preconditioning step. The bottom surface has been constrained in all directions, the remaining boundaries being constraint-free. This step permits to obtain the unloaded IVD equilibrium in which the initial osmotic pressure distribution and the unloaded IVD equilibrium swelling were established from the fixed charge density and the porosity initial fields ( $C_{fc0}$  and  $\phi_0$  table 2). The second step permits to simulate the head weight. A 100N creep-compressive force was applied on the top surface of the upper CEP in 8 minutes then remains constant until the equilibrium. Finally, starting from the result of the compression-creep step, we have applied a displacement-driven load to simulate the C6-C7 translations and rotations during a physiological cervical spine lateral bending, axial rotation, and flexion (Fig. 4). Data for C6-C7 kinematics in the cervical segment are obtained from in vivo measurements taken from the literature (table 1). To reproduce the experimental measurements, we have used a y-z-x sequence (corresponding to flexion/extension-axial rotation-lateral bending) to apply the C6-C7 rotations during spine movement. The center of rotation is the center of the most posterior

inferior point of the subjacent vertebrae (C7) for lateral bending and axial rotation [48, 49].  
For the flexion, the rotation center is the center of the subjacent vertebral body [50, 51].

## 2.6. Studied parameter range

The parametric study has been carried out by varying 10 parameters (table 2). For the NP and the AF ground substance tissues, the varied parameters were the shear modulus  $\mu$  defining the ECM stiffness, the first Lamé parameter  $\lambda$  defining its compressibility, and the initial permeability  $k_0$ . Collagen fiber network properties have also been studied by varying their rigidity  $a$ , their nonlinearity  $b$ , and their directions ( $\alpha_o$  and  $\alpha_i$ ). We have chosen the interval of variation of each parameter to be always in the range of values in previous numerical studies found in the literature (table 2). This choice permits testing the sensitivity of the IVD mechanical behavior to model parameters in extended ranges used in previous studies. It is important to mention that even if some cited studies do not use the same constitutive law as the actual work, they were used to define variation range for parameters equivalent to ours in their formulation. For example, we have used the value of  $a_{AF}$  in [52] even if this study does not take into consideration the fiber dispersion defined by  $K_{AF}$  in our model. We also calculated the equivalent  $\lambda_{NP}$  and  $\mu_{NP}$  from Young modulus and Poisson's ratio provided in [53] using elastic parameter conversion formulae.

For each parameter, the reference value was managed to be at the center of the studied range. The higher and the lower values were chosen in a way to be equally distant from the reference value and to form an interval that covers as many previously used values as possible. The first simulation has been performed using the reference parameter values (basic model). Then, for each test, we have varied only one parameter. Only the two fiber orientation angles have been simultaneously varied. To make this simultaneous variation simple we have fixed the mean fiber direction at  $35^\circ$  and defined the parameter  $\Delta\alpha$  which represents the difference

190 of the mean angle from inner and outer angles:  $\alpha_i = \pm(35 + \Delta\alpha)$  and  $\alpha_o = \pm(35 - \Delta\alpha)$ .  
191 Finally, 37 tests have been performed for each load type. A total of 1320h of computing time  
192 was needed in this study (about 220h with parallel computation) using an HPC cluster with  
193 28 cores and 128GB of RAM.

194

195 The studied outputs for the creep-compression step were the maximal NP pressure, the  
196 maximal normal stress, the axial and radial outflow rates, the final volume change, and the  
197 final axial displacement of the upper surface. For the physiological loads, we have studied the  
198 maximal normal and shear stress, the axial and radial outflow rates, the final volume change,  
199 and the final corresponding moment applied on the upper IVD surface. We have also studied  
200 the impact of model parameters on a global output which is the apparent stiffness for the  
201 different loads. The apparent stiffness for the rotational loads was calculated about the center  
202 of rotation (Appendix).

### 203 **3. Results**

#### 204 *3.1. Compression step*

205 During the compression step, we can differentiate two stages. The first one is the es-  
206 tablishment of the applied force. At this stage, the axial displacement pressurizes the fluid  
207 content due to the low permeability of the tissue. The IVD swells following this pressurization  
208 until the total establishment of the force. At this instant, the pressure and the radial swelling  
209 reach their maximal values. The second stage begins when the applied force is stabilized. In  
210 this stage, the water expulsion from the IVD becomes more important, the swelling decreases  
211 and the displacement of the loaded CEP continues until the equilibrium. We measured the  
212 influence of modifying the model parameters on the NP pressure, the normal stress, and the  
213 axial and radial flow rates at the end of the first stage. We studied also two equilibrium

214 results which are the volume loss caused by the water expulsion and the final displacement of  
 215 the loaded face which will determine the apparent stiffness of the IVD. With the basic model,  
 216 the relative change in IVD height was 4.8% and the relative change in its volume was 4.3%.  
 217 Figure 5 shows the effect of modifying the model parameters on the IVD response to com-  
 218 pression. Results show that the shear modulus of the AF ground substance  $\mu_{AF}$  is the most  
 219 influential parameter on IVD response to compressive load. The AF compressibility  $\lambda_{AF}$ ,  
 220 affects significantly the radial flow rate. This parameter has a lower influence on the axial  
 221 flow rate, the final displacement, and the volume loss but it contributes clearly to their deter-  
 222 mination. The NP and the AF permeabilities  $k_{0NP}$  and  $k_{0AF}$  play also an important role in  
 223 the pressurization stage. The pore pressure is very sensitive to the NP permeability and the  
 224 radial flow rate is highly influenced by the AF permeability. However, the permeabilities do  
 225 not contribute to the equilibrium state. Apart from the fiber rigidity, no noticeable influence  
 226 was found on fiber parameters. The reference apparent stiffness obtained with the basic model  
 227 was about  $337 Nmm^{-1}$ . This value depends on model parameters in a nearly linear way with  
 228 high sensitivity to the AF stiffness  $\mu_{AF}$  and less noteworthy dependency on fiber rigidity  $a_{AF}$   
 229 and AF compressibility  $\lambda_{AF}$ . No significant effect on the IVD apparent stiffness was found  
 230 for the other parameters.

### 231 3.2. Lateral bending

232 Figure 6 illustrates the influence of modifying model parameters on the IVD response to  
 233 lateral bending. The IVD normal stress, the axial flow rate, and the volume change in lateral  
 234 bending were dominated by the shear modulus of the AF ground substance  $\mu_{AF}$ . The radial  
 235 flow rate is highly sensitive to the AF permeability and depends less on  $\mu_{AF}$ . A less noticeable  
 236 dependency of the IVD outputs to the AF ground substance compressibility  $\lambda_{AF}$  was found.  
 237 Contrary to compression, we have noticed a significant dependency of the IVD behavior on

238 fiber parameters in lateral bending. The fiber non-linearity parameter  $b_{AF}$  has a crucial role  
 239 in the determination of the shear stress, the lateral bending moment, and the volume change.  
 240 Modifying the fiber rigidity  $a_{AF}$  has a noticeable effect on the same outputs. Although fiber  
 241 direction parameter  $\Delta\alpha$  has not the same importance in the IVD response to lateral bending,  
 242 we have found that varying this parameter may affect the shear stress and the radial outflow  
 243 rate. On the other hand, apart from  $\mu_{NP}$ , which slightly affects the radial flow rate, the NP  
 244 parameters varying in the study range has not a real influence on the IVD response to lateral  
 245 bending. The apparent stiffness in lateral bending found with the basic model was about  
 246  $16Nmrad^{-1}$ . This value is affected by modifying  $b_{AF}$  in the first row then AF stiffness  $\mu_{AF}$   
 247 and fiber rigidity  $a_{AF}$ . The dependency of the LB apparent stiffness to these parameters is  
 248 nonlinear.

### 249 3.3. Flexion

250 Figure 7 shows the influence of modifying model parameters on the IVD response respec-  
 251 tively to flexion. The studied outputs depend essentially on the fiber nonlinearity  $b_{AF}$  and  
 252 the AF ground substance shear modulus  $\mu_{AF}$ . A less significant effect of the fiber rigidity  
 253  $a_{AF}$  and orientation  $\Delta\alpha$  was found. The AF permeability  $k0_{AF}$  has a significant effect on  
 254 the radial flow rate value. The AF ground substance compressibility  $\lambda_{AF}$  contributes to the  
 255 determination of the normal stress and the volume change. In a similar way to lateral bend-  
 256 ing, apart from  $\mu_{NP}$ , varying the NP parameters in the study range does not affect the IVD  
 257 response to flexion. The apparent stiffness in lateral bending found with the basic model was  
 258 about  $4.4Nmrad^{-1}$ . The flexion apparent stiffness depends, in a nonlinear way, on  $b_{AF}$ ,  $\mu_{AF}$   
 259 and  $a_{AF}$  in descending order.

### 260 3.4. Axial rotation

261 The results of the effect of modifying model parameters on IVD response to axial rotation  
262 are shown in figure 8. As for the other types of load, varying  $\mu_{AF}$  has a high effect on the  
263 maximal stress and the flow rates in axial rotation. In addition, the permeability of the AF  
264 slightly contributes to the determination of the radial flow rate where the role of NP per-  
265 meability remains negligible. The fiber parameters  $b_{AF}$  and  $a_{AF}$  role remains crucial in the  
266 determination of shear stress, the axial rotation moment, and the volume change. We note  
267 that fiber orientation contributes more significantly to the IVD response to axial rotation than  
268 its contribution to flexion and lateral bending. Similarly to the two latter motion results, the  
269 apparent stiffness value is dominated by  $b_{AF}$ ,  $\mu_{AF}$  and  $a_{AF}$  with a more noticeable effect of  
270 the NP shear modulus  $\mu_{NP}$ . The axial rotation apparent stiffness value found with the basic  
271 parameters was  $2.83Nmrad^{-1}$ .

272 The apparent stiffness values found with the three physiological rotations are significantly  
273 smaller than the apparent stiffness computed with  $2Nm$  pure moments applied in the valida-  
274 tion study with ( $25.8Nmrad^{-1}$  in lateral bending,  $15.3Nmrad^{-1}$  in flexion, and  $24.9Nmrad^{-1}$   
275 in axial rotation). This comparison reveals that coupling the different rotations and trans-  
276 lations during a physiological movement, together with the specific anisotropic hyperelastic  
277 properties of the IVD, help reduce the resulting moment that is necessary to turn the head.

## 278 4. Discussion

279 This study was aimed to answer a key question that precedes any study treating the IVD  
280 mechanical modeling: given the data set and objectives, to which mechanical parameters  
281 specific attention should be paid? The answer to this question permits reducing the model  
282 numerical cost by considering the appropriate assumptions or by reducing the number of pa-  
283 rameters in the identification studies. To prioritize model parameters we have conducted a

parametric study using an anisotropic poro-hyperelastic model of the IVD and we have examined the effect of varying 10 parameters, in the literature range, on the model response to physiological day-to-day loads.

Our methodology in the definition of parameters range has been oriented to cover the most used values in literature. Therefore, it does not consist of a sensibility study where we try to find the effect of each parameter on a limited interval but of a parametric study where we have examined the parameters contribution to the IVD behavior based on the variety of these parameter values used by previous works. Although this choice imposes a very varied width of parameters range, it allows examining the utility of using very high or very low parameter values compared to the most commonly used order of magnitude. For example, the common value of  $b_{AF}$  is under 200 in the most studies [54, 52, 11, 55] but it takes a value of 300 in [56] and 1045 in [8]. The high dependency of our model on the value of  $b_{AF}$  can be explained by the use of those two extreme values.

Our study outlines the out most influence of changing the stiffness of the extracellular matrix of AF on the poro-hyperelastic behavior of the cervical disc, by taking into account creep compression, physiological relaxation movements during flexion, bending and axial rotation. It is important to cite that we have faced numerical processing issues when using a low value of  $\mu_{AF}$  and we suggest using  $\mu_{AF} \geq 0.8MPa$  for the same type of model. In the current study, we have found that even the AF compressibility parameters  $\lambda_{AF}$  had a relevant role in the determination of many output results. This influence highlights the necessity of using a compressible extracellular matrix in FE models. These results can explain why many studies using a nearly incompressible model for the IVD are validated with a low bulk modulus which does not satisfy the near incompressibility assumption for the AF (1.45 MPa in [57], 0.8 to 1.4 MPa in [11] and 0.67 MPa in [58]). Moreover, very few studies take into account transverse deformation to the traction direction, which are crucial to estimate the compressible behavior



309 of AF [59, 60, 61, 29, 30]. The last two experimental studies have clearly outlined, on bovine  
 310 and porcine disks respectively, the auxetic behavior of AF, and both report the dependency  
 311 of the apparent Poisson's ratios to the deformation amplitude, with negative Poisson's ratios  
 312 in the circumferential radial plane. Therefore, on the compressible behavior of the AF, we  
 313 conclude that more experimental, numerical, and theoretical studies are needed to understand  
 314 the complex, non-linear auxetic behavior of the AF. On the other hand, the relevance of the  
 315  $\lambda_{NP}$  has not been shown in the current study. We think that the role of this parameter was  
 316 hidden by its small range of study (0.1 to 0.5MPa). However, the compressible behavior  
 317 of the human NP has been clearly outlined in several experimental studies [62, 63]. This  
 318 incites us to suggest using a compressible swelling material for the NP to catch its mechanical  
 319 behavior except at very high strain rates or under dynamic conditions where a viscoelastic  
 320 incompressible behavior could be sufficient [64, 65, 66].

321 As we have shown, the permeabilities of the AF and the NP do not contribute to the  
 322 determination of the equilibrium state. However, the radial flow rates are sensitive to AF  
 323 permeability and less sensitive to NP permeability. The latter contributes more to the de-  
 324 termination of the pore pressure. It is known that the water exchange within the IVD is a  
 325 key factor for nutrient transport and cell activity. Therefore, inaccurate estimation of the  
 326 permeabilities, especially of the AF, may lead to a loss of sufficiency in the biomechanical  
 327 models of treating degeneration and growth. The current strain-dependent permeability laws  
 328 proposed by [34] and [67] are sufficient to investigate the IVD solid-like behavior as reported  
 329 by many studies. However, given their isotropic formulation, they are not able to describe  
 330 precisely the water exchange rate in the fiber-reinforced tissues like AF [11]. We anticipate  
 331 that a more accurate permeability expression that depends on strain but also on collagen fiber  
 332 network organization will have a higher impact on water flow rates.

333 Another important finding is that collagen fiber properties including rigidity, nonlinearity,

334 and orientation have no significant effect on the response of the IVD to compression. How-  
 335 ever, they are a determinant factor in the cases of flexion, lateral bending, and axial rotation.  
 336 As mentioned previously, the high dependency of IVD behavior to the value of  $b_{AF}$  may be  
 337 partially caused by the large difference between its higher and lower tested values. The fiber  
 338 nonlinearity parameter is not a measurable property which makes it difficult to estimate.  
 339 Therefore, on  $b_{AF}$  value, we suggest performing more oriented AF local identification studies  
 340 to limit the range of variation of this parameter. Collagen fibers have high stiffness but they  
 341 do not contribute to the mechanical behavior only when they are in tension. Contrary to  
 342 compression, in the case of rotational motion, the strain principal directions are near to the  
 343 fiber orientation angles due to the large torsion deformation, especially in axial rotation. This  
 344 result comes back to the results of [34, 68] and [69] affirming that isotropic models are able to  
 345 reproduce the IVD response to compression. However, as underlined by [21], it is essential to  
 346 consider fiber reinforcement when studying the IVD behavior in axial rotation. Furthermore,  
 347 collagen network architecture should be neatly described by namely regional orientation dif-  
 348 ference between inner/outer and posterior/anterior AF.

349 This study also revealed that the collagen network within the AF has a crucial role to  
 350 optimize the necessary resulting moment to turn the head. In combination with the relative  
 351 movements of the adjacent vertebrae during axial rotation, lateral bending, and flexion, the  
 352 mechanical properties of the collagen fiber network appear to be particularly well adapted to  
 353 reduce the resulting moment by an order of magnitude compared to pure rotations. This key  
 354 feature has to be taken into account while designing IVD implants.

355 To take back the main aim of this study, we suggest simplifying IVD model validation  
 356 studies by reducing the number of identified parameters depending on the experimental opti-  
 357 mization objective and load type. (1) For tests in statics, very slow loading tests, and when  
 358 the experimental object is not time-dependent such as force-displacement curve, there is no

359 need to identify the permeability value. (2) For fiber-reinforced models, fiber orientation and  
360 nonlinearity should not be included in the identified parameter except when studying IVD  
361 response to rotational motion. Fiber rigidity is a determinant parameter for all types of load.  
362 (3) None of the mechanical parameters of the extracellular matrix of the AF could be ne-  
363 glected in the identification process. High attention should be paid to the determination of  
364 the stiffness of the AF ground substance.

365 Some sources of uncertainty could be identified from the current results. On a numerical level,  
366 the results of this study are provided without focusing on the uncertainty quantification of  
367 each parameter in the validation step. However, we can identify some parameters with infi-  
368 nite uncertainty such as the two permeabilities for stationary analysis or the fiber orientation  
369 for the uniaxial load. In the identification studies, the accuracy of the model needs to be  
370 investigated by uncertainty quantification. This will be useful to localize the optimal exper-  
371 imental fields to measure, design accurate experiments and therefore minimize model error  
372 [72, 73, 74]. On a physiological level, only the IVD prestress related to the osmotic pressure  
373 was included. However, a second part, related to the gradient of tissue growth could be taken  
374 into account. The IVD prestress was studied for bovine and porcine tissues [75, 76, 77, 29] but  
375 no data concerning human disc prestress are yet provided in the literature to our knowledge.  
376 In addition, the loading conditions, taken from previous experimental studies, may affect the  
377 current results given the non linear anisotropic behavior of the model.

378 Our study, which focused on varying each parameter independently of the others, revealed  
379 the complex mechanical behavior in in-vivo solicitations. In future work, the variation of mul-  
380 tiple parameters at the same time will be performed. We anticipate this scheme may reveal  
381 coupled effects and allow more efficient simplifications of the validation studies.

$\sigma$	Total Cauchy stress tensor
$\sigma^e$	Solid phase effective stress tensor
$C$	Right Cauchy-Green strain
$\vec{e}_i$	Director vector of the $i^{th}$ fiber family
$p$	Fluid phase hydrostatic pressure ( $Pa$ )
$\Delta\pi$	Osmotic pressure ( $Pa$ )
$k_0$	initial permeability ( $m^4 N^{-1} s^{-1}$ )
$C_{fc}$	Fixed charge density ( $mol\ m^{-3}$ )
$C_{fc0}$	Initial fixed charge density ( $mol\ m^{-3}$ )
$\phi_0$	Initial porosity (unitless)
$J$	Deformation gradient determinant
$\mu$	Shear modulus ( $Pa$ )
$\lambda$	First Lamé parameter ( $Pa$ )
$a_i$	Fiber rigidity ( $Pa$ )
$b_i$	Fiber non linearity coefficient (unitless)
$K$	Fiber dispersion coefficient (unitless)
$I_{fi}$	Direction invariant of the $i^{th}$ family fiber
$\alpha_i$	Inner fiber orientation ( $^\circ$ )
$\alpha_o$	Outer fiber orientation ( $^\circ$ )
$\Delta\alpha$	$(\alpha_i - \alpha_o)/2$ ( $^\circ$ )

$R$  universal gaz constant  $=8.314J \text{ mol}^{-1}.K^{-1}$

$T$  Absolute temperature  $=310K$

385  $C_e$  External salt concentration  $=150mol \text{ m}^{-3}$

$\varphi_i$  Internal osmotic coefficient  $=0.9$

$\varphi_e$  External osmotic coefficient $=0.9$

## 386 **Appendix: Apparent stiffness**

The head-weight force in compression and the coupled displacements in the other physiological loads were applied on the upper surface of the disc which is assumed to be rigid. The apparent stiffness is calculated using the applied load or displacement and the resulting displacement or external force, respectively. For compression, the apparent stiffness  $A_{pp}S(Nm^{-1})$  is defined as:

$$A_{pp}S = \left| \frac{F_{app}}{w_{res}} \right|$$

where  $F_{app}(N)$  is the applied force and  $w_{res}(m)$  is the displacement of the upper surface in the  $z$  direction (the same direction as the applied force).

For the other physiological loads, the apparent stiffness  $A_{pp}S(Nm \text{ rad}^{-1})$  is defined as:

$$A_{pp}S = \left| \frac{\vec{M}_{res} \cdot \vec{e}_p}{\varphi_{app}} \right|$$

where  $\vec{M}_{res}(Nm)$  is the global moment of the upper surface points about the center of rotation,  $\varphi_{app}(rad)$  is the global cervical segment rotation as described in the table 1 and  $\vec{e}_p$  the principal direction of the rotation:  $\vec{x}$  for flexion,  $\vec{y}$  for lateral bending and  $\vec{z}$  for axial rotation.  $M_{res}(Nm)$  is obtained according to this equation:

$$\vec{M}_{res} = \iint_{up} \vec{M}_{n,res} dS = \iint_{up} \left( O\vec{M}_n \wedge \vec{F}_{n,res} \right) dS$$

387 where  $\vec{M}_{n,res}(Nm)$  is the resulting nodal moment,  $\vec{F}_{n,res}(N)$  the resulting nodal force, and  
388  $O\vec{M}_n(m)$  the final nodal position with regard to the center of rotation.

### 389 **Conflict of interests**

390 The authors declare that they have no conflict of interests to disclose.

### 391 **Ethical approval**

392 Not required

### 393 **Source of funding**

394 This work has been supported by MESO@LR Platform of the University of Montpel-  
395 lier, by Labex NUMEV (ANR-10-LABX-20 projects 2017-1-27) and by CNRS (AAP "Osez  
396 l'interdisciplinarité 2018", MoTiV Project)

### 397 **References**

- 398 [1] Zhuang Y, Huang B, Li CQ, Liu LT, Pan Y, Zheng WJ, Luo G, Zhou Y. Construction  
399 of tissue-engineered composite intervertebral disc and preliminary morphological and  
400 biochemical evaluation. *Biochem Biophys Res Commun* 2011;407(2):327–32.
- 401 [2] D’Este M, Eglin D, Alini M. Lessons to be learned and future directions for intervertebral  
402 disc biomaterials. *Acta Biomater* 2018;78:13–22.
- 403 [3] Buckley CT, Hoyland JA, Fujii K, Pandit A, Iatridis JC, Grad S. Critical aspects and  
404 challenges for intervertebral disc repair and regeneration-harnessing advances in tissue  
405 engineering. *JOR Spine* 2018;1(3):e1029.

- [4] Sharabi M, Wertheimer S, Wade KR, Galbusera F, Benayahu D, Wilke HJ, Haj-Ali R. Towards intervertebral disc engineering: Bio-mimetics of form and function of the annulus fibrosus lamellae. *J Mech Behav Biomed Mater* 2019;94:298–307.
- [5] Guo LX, Fun W. Impact of material properties of intervertebral disc on dynamic response of the human lumbar spine to vertical vibration: A finite element sensitivity study. *Med Biol Eng Comput* 2019;57(1):221–9.
- [6] Hollingsworth NT, Wagner DR. Modeling shear behavior of the annulus fibrosus. *J Mech Behav Biomed Mater* 2011;4(7):1103–14.
- [7] Reutlinger C, Bürki A, Brandejsky V, Ebert L, Büchler P. Specimen specific parameter identification of ovine lumbar intervertebral discs: On the influence of fibre-matrix and fibre-fibre shear interactions. *J Mech Behav Biomed Mater* 2014;30:279–89.
- [8] Mengoni M, J. Luxmoore BJ, N. Wijayathunga VN, Jones AC, Broom ND, Wilcox RK. Derivation of inter-lamellar behaviour of the intervertebral disc annulus, *J Mech Behav Biomed Mater* 2015;48:164–72.
- [9] Masni-Azian, Tanaka M. Biomechanical investigation on the influence of the regional material degeneration of an intervertebral disc in a lower lumbar spinal unit: A finite element study. *Comput Biol Med* 2018;98:26–38.
- [10] Oreskes N. Evaluation (not validation) of quantitative models. *Environ Health Perspect* 1998;106:1453–1460.
- [11] Chetoui MA, Boiron O, Ghiss M, Dogui A, Deplano V. Assessment of intervertebral disc degeneration-related properties using finite element models based on  $\rho_h$ -weighted MRI data. *Biomech Model Mechanobiol* 2019;18(1):17–28.

- [12] Olson SA, Marsh JL, Anderson DD, Latta Pe LL. Designing a biomechanics investigation: choosing the right model. *J Orthop Trauma* 2012;26(12):672-7.
- [13] Urcun S, Rohan PY, Sciumè G, Bordas SPA. Cortex tissue relaxation and slow to medium load rates dependency can be captured by a two-phase flow poroelastic model. *J Mech Behav Biomed Mater* 2022;126:104952.
- [14] Stadelmann MA, Maquer G, Voumard B, Grant A, Hackney DB, Vermathen P, Alkalay RN, Zysset PK. Integrating MRI-based geometry, composition and fiber architecture in a finite element model of the human intervertebral disc. *J Mech Behav Biomed Mater* 2018;85:37–42.
- [15] Thakolkaran P, Joshi A, Zheng Y, Flaschel M, De Lorenzis L, Kumar S. NN-EUCLID: Deep-learning hyperelasticity without stress data. In: Pre-print under review (2022). arXiv: 2205.06664.
- [16] Krokos V, Bui Xuan V, Bordas SPA, Young P, Kerfriden P. A Bayesian multiscale CNN framework to predict local stress fields in structures with microscale features. *Comput Mech* 2022;69:733–66.
- [17] Deshpande S, Lengiewicz J, Bordas SP. Probabilistic deep learning for real-time large deformation simulations. *Comput Methods Appl Mech Eng* 2022;398:115307.
- [18] Anderson AE, Ellis BJ, Weiss JA. Verification, validation and sensitivity studies in computational biomechanics. *Comput Methods Biomech Biomed Eng* 2007;10(3):171–84.
- [19] Malandrino A, Planell JA, Lacroix D, Statistical factorial analysis on the poroelastic material properties sensitivity of the lumbar intervertebral disc under compression, flexion and axial rotation. *J Biomech* 2006;42(16):2780–88.



- [20] Jebaseelan DD, Jebaraj C, Yoganandan N, Rajasekaran S, Kanna RM. Sensitivity studies of pediatric material properties on juvenile lumbar spine responses using finite element analysis. *Med Biol Eng Comput* 2012;50(5):515–22.
- [21] Yang B, O’Connell GD. Effect of collagen fiber orientation on intervertebral disc torsion mechanics. *Biomech Model Mechanobiol* 2017;16(6):2005–15.
- [22] Zander T, Dreischarf M, Timm AK, Baumann WW, Schmidt H. Impact of material and morphological parameters on the mechanical response of the lumbar spine – a finite element sensitivity study. *J Biomech* 2017;53:185–90.
- [23] Kumaresan S, Yoganandan N, Pintar FA. Finite element analysis of the cervical spine: A material property sensitivity study. *Clin Biomech* 1999;14(1):41–53.
- [24] Ng HW, Teo EC, Lee VS. Statistical factorial analysis on the material property sensitivity of the mechanical responses of the C4-C6 under compression, anterior and posterior shear. *J Biomech* 2004;37(5):771–7.
- [25] Duprez M, Bordas SPA, Bucki M, Bui HP, Chouly F, Lleras V et al. Quantifying discretization errors for soft tissue simulation in computer assisted surgery: A preliminary study. *Applied Mathematical Modelling* 2020;77:709–23.
- [26] Anderst W, Donaldson W, Lee J, Kang J. Cervical Spine Disc Deformation During In Vivo Three-Dimensional Head Movements. *Ann Biomed Eng* 2016;44(5):1598-612
- [27] Sharabi M, Wade K, Haj-Ali R. The Mechanical Role of Collagen Fibers in the Intervertebral Disc. In: Galbusera F, Wilke HJ, editors. *Biomechanics of the Spine*, Academic Press;2018, p. 105–23
- [28] Yang B, O’Connell GD. Swelling of fiber-reinforced soft tissues is affected by fiber ori-

entation, fiber stiffness, and lamella structure. *Journal of the Mechanical Behavior of Biomedical Materials* 2018;82:320–8.

[29] Dusfour G, Maumus M, Cañadas P, Ambard D, Jorgensen D, Noël D, Le Floc’h S. Mesenchymal stem cells-derived cartilage micropellets: A relevant in vitro model for biomechanical and mechanobiological studies of cartilage growth. *Mater Sci Eng: C* 2020;112:110808.

[30] Derrouiche A, Karoui A, Zaïri F, Ismail J, Qu Z, Chaabane M, Zaïri F. The two poisson’s ratios in annulus fibrosus: Relation with the osmo-inelastic features. *Mech Soft Mater* 2020;2:1.

[31] Mow VC, Kuei SC, Lai WM, Armstrong CG. Biphasic creep and stress relaxation of articular cartilage in compression: Theory and experiment. *J Biomech Eng* 1980;102(1):73–84.

[32] Lanir Y. Biorheology and fluid flux in swelling tissues. I. Bicomponent theory for small deformations, including concentration effects. *Biorheology* 1987;24(2):173–87.

[33] Wilson W, Donkelaar CV, Huyghe JM, Armstrong CG. A comparison between mechano-electrochemical and biphasic swelling theories for soft hydrated tissues. *J Biomech Eng* 2005;127(1):158–65.

[34] Argoubi M, Shirazi-Adl A. Poroelastic creep response analysis of a lumbar motion segment in compression. *J Biomech* 1996;29(10):1331–9.

[35] Gasser T, Ogden R, Holzapfel G. Hyperelastic modelling of arterial layers with distributed collagen fibre orientation. *J Roy Soc Interface* 2006;3(6):15–35.

[36] Gilad I, Nissan M. A study of vertebra and disc geometric relations of the human cervical and lumbar spine. *Spine* 1986;11(2):154–7.

- [37] Frobin W, Leivseth G, Biggemann M, Brinckmann P. Vertebral height, disc height, posteroanterior displacement and dens-atlas gap in the cervical spine: Precision measurement protocol and normal data. *Clin Biomech* 2002;17(6):423–31.
- [38] Wiegand R, Kettner NW, Brahee D, Marquina N. Cervical spine geometry correlated to cervical degenerative disease in a symptomatic group. *J Manip and Physiol Ther* 2003;26(6):341–6.
- [39] Pitzen T, Schmitz B, Georg T, Barbier D, Beuter T, Steudel WI, Reith W. Variation of endplate thickness in the cervical spine, *Eur Spine J* 2004;13(3):235–40.
- [40] Lou J, Liu H, Rong X, Li H, Wang B, Gong Q. Geometry of inferior endplates of the cervical spine. *Clinical Neurology And Neurosurgery* 2016;142:132–6.
- [41] Yu Y, Mao H, Li JS, Tsai TY, Cheng L, Wood KB, et al. Ranges of cervical intervertebral disc deformation during an in vivo dynamic flexion-extension of the neck. *J Biomech Eng* 2017;139(6):0645011–7.
- [42] Geuzaine C, Remacle J. Gmsh: A 3-D finite element mesh generator with built-in pre- and post-processing facilities. *Int J Num Meth Eng* 2009;79(11):1309–31.
- [43] Dubois F, Jean M, Renouf M, Mozul R, Martin A, Bagn  ris M. Lmgc90. CSMA 2011, Giens, France. hal-00596875. doi:[www.git-xen.lmgc.univ-montp2.fr/lmgc90/lmgc90\\\_user/wikis/home](http://www.git-xen.lmgc.univ-montp2.fr/lmgc90/lmgc90\_user/wikis/home).
- [44] Holzapfel GA, Schulze-Bauer CA, Feigl G, Regitnig P. Single lamellar mechanics of the human lumbar annulus fibrosus. *Biomech Model Mechanobiol* 2005;3(10):125–40.
- [45] Yoganandan N, Pintar FA, Stemper BD, Wolfla CE, Shender BS, Paskoff G. Level-dependent coronal and axial moment-rotation corridors of degeneration-free cervical spines in lateral flexion. *J bone and joint surgery* 2007;89(5):1066–74.

- [46] Wheeldon JA, Pintar FA, Knowles S, Yoganandan N. Experimental flexion/extension data corridors for validation of finite element models of the young, normal cervical spine. *J Biomech* 2006;39(6):375–80.
- [47] Yoganandan N, Stemper BD, Pintar FA, Baisden JL, Shender BS, Paskoff G. Normative segment-specific axial and coronal angulation corridors of subaxial cervical column in axial rotation 2008; *Spine* 33(5):490–6.
- [48] Ishii T, Mukai Y, Hosono N, Sakaura H, Fujii R, Nakajima Y, Tamura Y, Iwasaki M, Yoshikawa H, Sugamoto K. Kinematics of the cervical spine in lateral bending: In vivo three-dimensional analysis. *Spine* 2006;31(2):155–60.
- [49] Lin CC, Lu TW, Wang TM, Hsu CY, Hsu SJ, Shih TF. In vivo three-dimensional intervertebral kinematics of the subaxial cervical spine during seated axial rotation and lateral bending via a fluoroscopy-to-CT registration approach. *J Biomech* 2014;47(13):3310–7.
- [50] Crawford N, Yamaguchi G, Dickman C. Methods for determining spinal flexion/extension, lateral bending, and axial rotation from marker coordinate data: Analysis and refinement. *Human Movement Sci* 1996;15(1):55–78.
- [51] Anderst WJ, Donaldson WF 3rd, Lee JY, Kang JD. Three-dimensional intervertebral kinematics in the healthy young adult cervical spine during dynamic functional loading. *J Biomech* 2015;48(7):1286–93.
- [52] Jacobs NT, Cortes DH, Peloquin JM, Vresilovic EJ, Elliott DM. Validation and application of an intervertebral disc finite element model utilizing independently constructed tissue-level constitutive formulations that are nonlinear, anisotropic, and time-dependent. *J Biomech* 2014;47(11):2540–6.

- 539 [53] Ferguson SJ, Ito K, Nolte LP. Fluid flow and convective transport of solutes within the  
540 intervertebral disc. *J Biomech* 2004;37(2):213–21.
- 541 [54] Ayturk UM, Gadowski B, Schuldt D, Patel V, Puttlitz CM. Modeling degenerative disk  
542 disease in the lumbar spine: a combined experimental, constitutive, and computational  
543 approach. *J Biomech eng* 2012;134(10):101003.
- 544 [55] Honegger JD, Actis J, Gates DH, Silverman AK, Munson AH, Petrella AJ. Development  
545 of a multiscale model of the human lumbar spine for investigation of tissue loads in  
546 people with and without a transtibial amputation during sit-to-stand. *Biomech Model*  
547 *Mechanobiol* 2021;20(1):339–58.
- 548 [56] Castro AP, Wilson W, Huyghe JM, Ito K, Alves JL. Intervertebral disc creep behavior  
549 assessment through an open source finite element solver. *J Biomech* 2014;47(1):297–301.
- 550 [57] Schmidt H, Reitmaier S, Is the ovine intervertebral disc a small human one? A finite  
551 element model study, *J Mech Behav Biomed Mater* 2013;17:229–41.
- 552 [58] Galbusera F, Schmidt H, Noailly J, Malandrino A, Lacroix D, Wilke HJ, Shirazi-Adl A.  
553 Comparison of four methods to simulate swelling in poroelastic finite element models of  
554 intervertebral discs. *J Mech Behav Biomed Mater* 2011;4(7):1234–41.
- 555 [59] Acaroglu ER, Iatridis JC, Setton LA, Foster RJ, Mow VC, Weidenbaum M. Degener-  
556 ation and aging affect the tensile behavior of human lumbar annulus fibrosus. *Spine*  
557 1995;20(24):2690–701.
- 558 [60] Elliott DM, Setton LA. Anisotropic and inhomogeneous tensile behavior of the human  
559 annulus fibrosus: Experimental measurement and material model predictions. *J Biomech*  
560 *Eng* 2001;123(3):256–63.

- [61] Baldit A, Ambard D, Cherblanc F, Royer P. Experimental analysis of the transverse mechanical behaviour of annulus fibrosus tissue. *Biomech Model Mechanobiol* 2014;13(3):643–52.
- [62] Cloyd JM, Malhotra NR, Weng L, Chen W, Mauck RL, Elliott DM. Material properties in unconfined compression of human nucleus pulposus, injectable hyaluronic acid-based hydrogels and tissue engineering scaffolds. *Eur Spine J* 2007;16(11):1892–8.
- [63] Johannessen W, Elliott DM. Effects of degeneration on the biphasic material properties of human nucleus pulposus in confined compression. *Spine* 2005;30(24):E724–9.
- [64] Iatridis JC, Weidenbaum M, Setton LA, Mow VC. Is the nucleus pulposus a solid or a fluid? mechanical behaviors of the nucleus pulposus of the human intervertebral disc. *Spine* 1996;21(10):1174–84.
- [65] Iatridis JC, Setton LA, Weidenbaum M, Mow VC, The viscoelastic behavior of the non-degenerate human lumbar nucleus pulposus in shear. *J Biomech* 1997;30(10):1005–13.
- [66] Leahy JC, Hukins DWL. Viscoelastic properties of the nucleus pulposus of the intervertebral disk in compression. *J Mater Sci: Mater Med* 2001;12(8):689–92.
- [67] Gu WY, Yao H, Huang CY, Cheung HS. New insight into deformation-dependent hydraulic permeability of gels and cartilage, and dynamic behavior of agarose gels in confined compression. *J Biomech* 2003;36(4):593–8.
- [68] Cortes DH, Jacobs NT, DeLucca JF, Elliott DM. Elastic, permeability and swelling properties of human intervertebral disc tissues: A benchmark for tissue engineering. *J Biomech* 2014;47(9):2088–94.
- [69] Chetoui MA, Boiron O, Dogui A, Deplano V. Prediction of intervertebral disc mechanical

583 response to axial load using isotropic and fiber reinforced FE models. *Comput Methods*  
584 *Biomech Biomed Eng* 2017;20:S39–S40.

585 [70] Ruiz C, Noailly J, Lacroix D. Material property discontinuities in intervertebral disc  
586 porohyperelastic finite element models generate numerical instabilities due to volumetric  
587 strain variations. *J Mech Behav Biomed Mater* 2013;26:1–10.

588 [71] Lu Y, Maquer G, Museyko O, Püschel K, Engelke K, Zysset P, Morlock M, Huber G.  
589 Finite element analyses of human vertebral bodies embedded in polymethylmethacrylate  
590 or loaded via the hyperelastic intervertebral disc models provide equivalent predictions  
591 of experimental strength. *J Biomech* 2014;47(10):2512–6.

592 [72] Sutula D, Elouneq A, Sensale M, Chouly F, Chambert J, Lejeune A et al. An open source  
593 pipeline for design of experiments for hyperelastic models of the skin with applications  
594 to keloids. *J Mech Behav Biomed Mater* 2020; 112:103999

595 [73] Elouneq A, Sutula D, Chambert J, Lejeune A, Bordas SPA, Jacquet E. An open-source  
596 FEniCS-based framework for hyperelastic parameter estimation from noisy full-field data:  
597 Application to heterogeneous soft tissues. *Computers & Structures* 2021;255:106620

598 [74] Mazier A, Bilger A, Forte AE, Peterlik I, Hale JS, Bordas SPA. Inverse deformation anal-  
599 ysis: an experimental and numerical assessment using the FEniCS Project. *Engineering*  
600 *with Computers* 2022. <https://doi.org/10.1007/s00366-021-01597-z>.

601 [75] Duclos SE, Michalek AJ. Residual strains in the intervertebral disc annulus fibrosus  
602 suggest complex tissue remodeling in response to in-vivo loading. *J Mech Behav Biomed*  
603 *Mater* 2017;68:232—238

604 [76] Mengoni M, Kayode O, Sikora SNF, Zapata-Cornelio FY, Gregory DE, Wilcox RK.

605 Annulus fibrosus functional extrafibrillar and fibrous mechanical behaviour: experimental  
606 and computational characterisation. R Soc Open Sci 2017;4(8):170807

607 [77] Michalek AJ, Gardner-Morse MG, Iatridis JC. Large residual strains are present in the  
608 intervertebral disc annulus fibrosus in the unloaded state. J Biomech 2012;45(7):1227-31



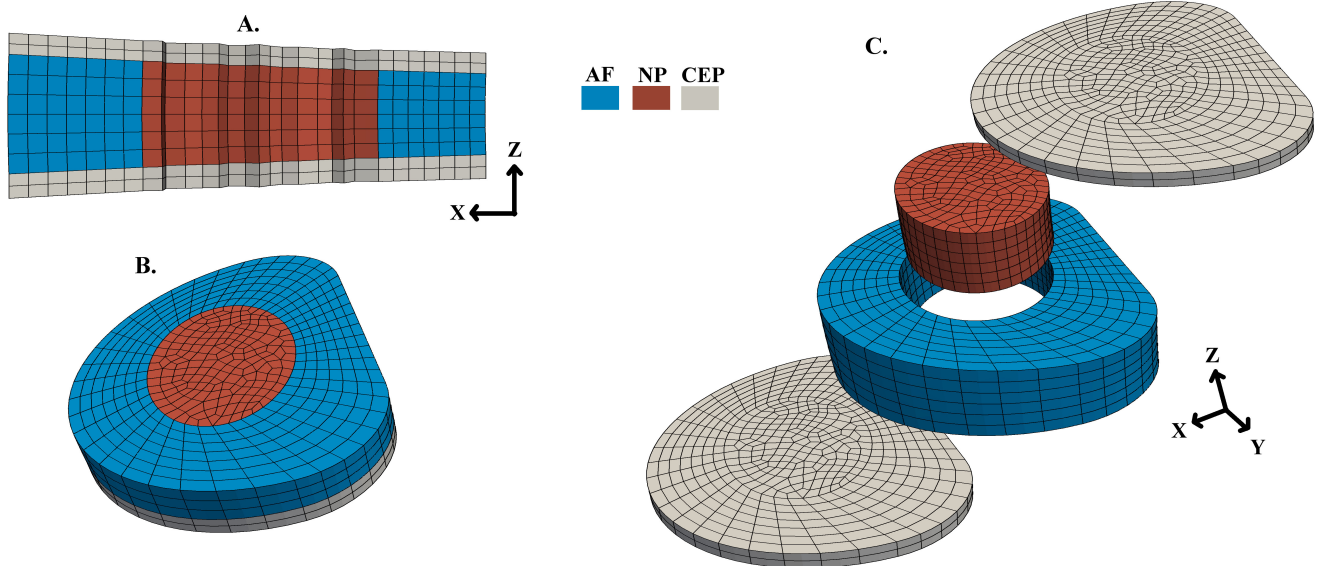


Figure 1: Geometry of C6-C7 IVD. A. Sagittal section. B. Transverse section. C. Exploded view.

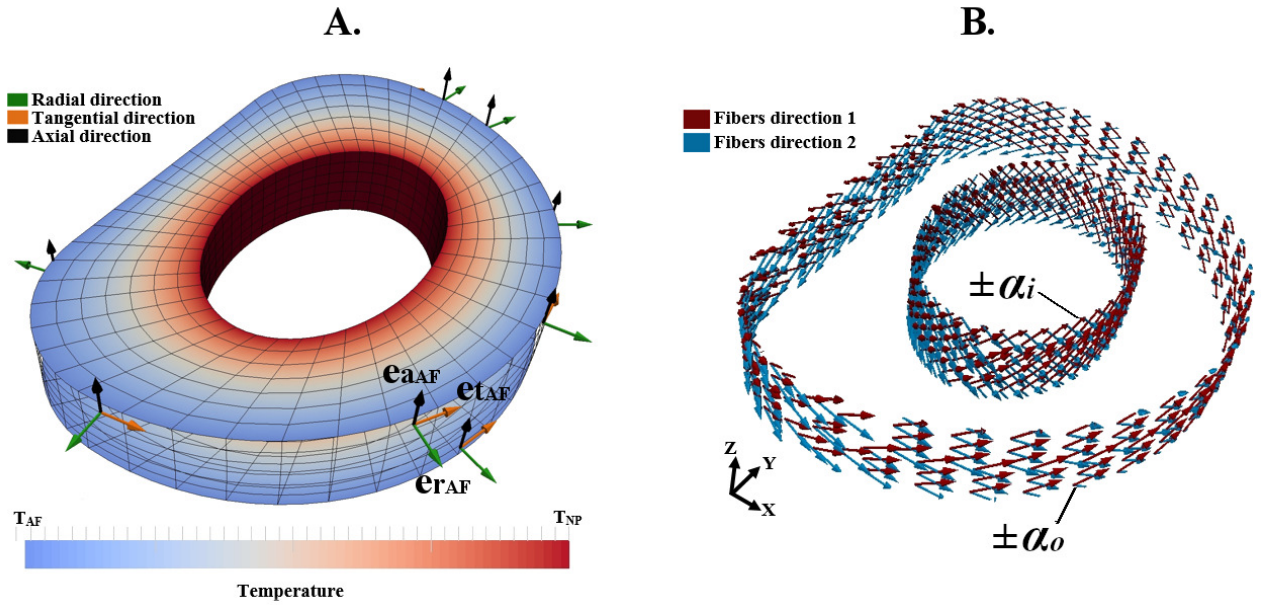


Figure 2: Definition of fiber orientation. A. Thermal solution and definition of the new coordinate system. B. Fibers directions in the inner and the outer lamellae of the AF

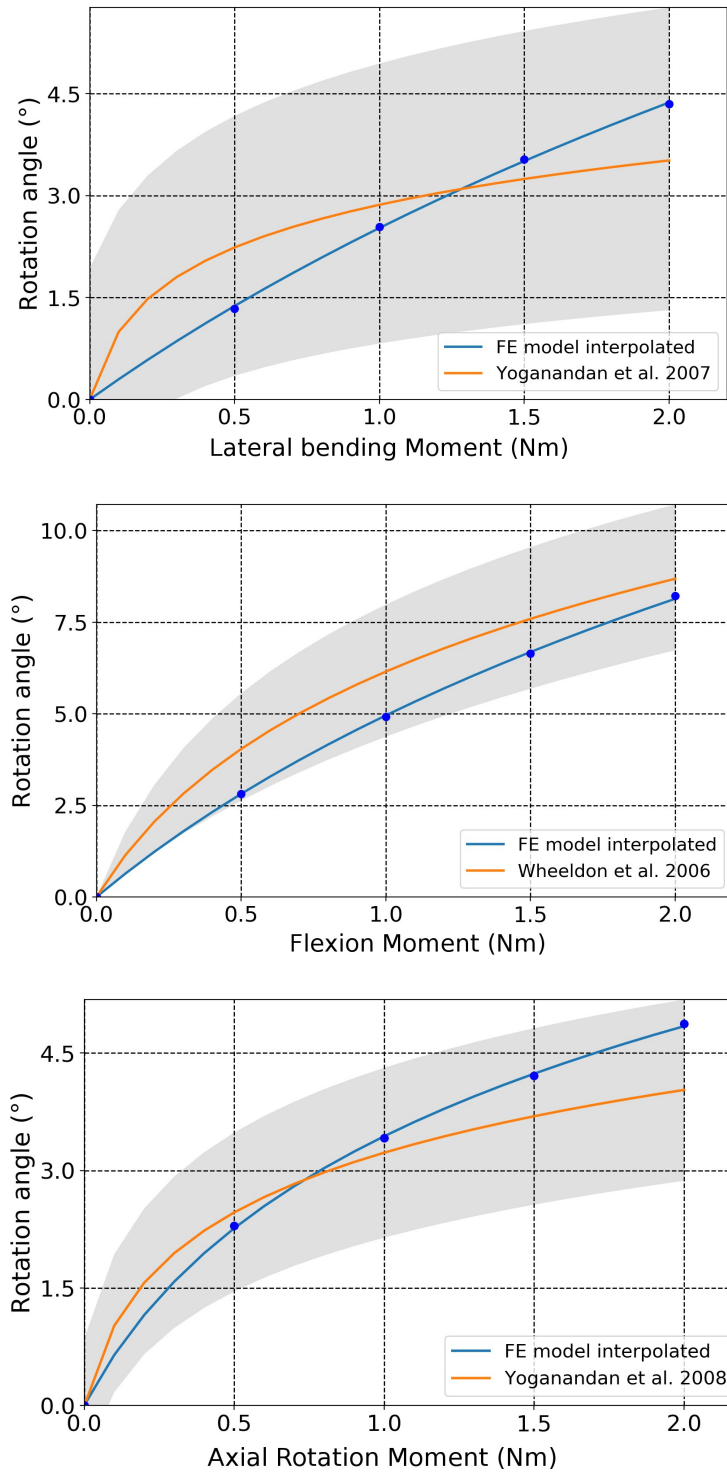


Figure 3: Experimental vs numerical response of the C6-C7 IVD to a pure moment load

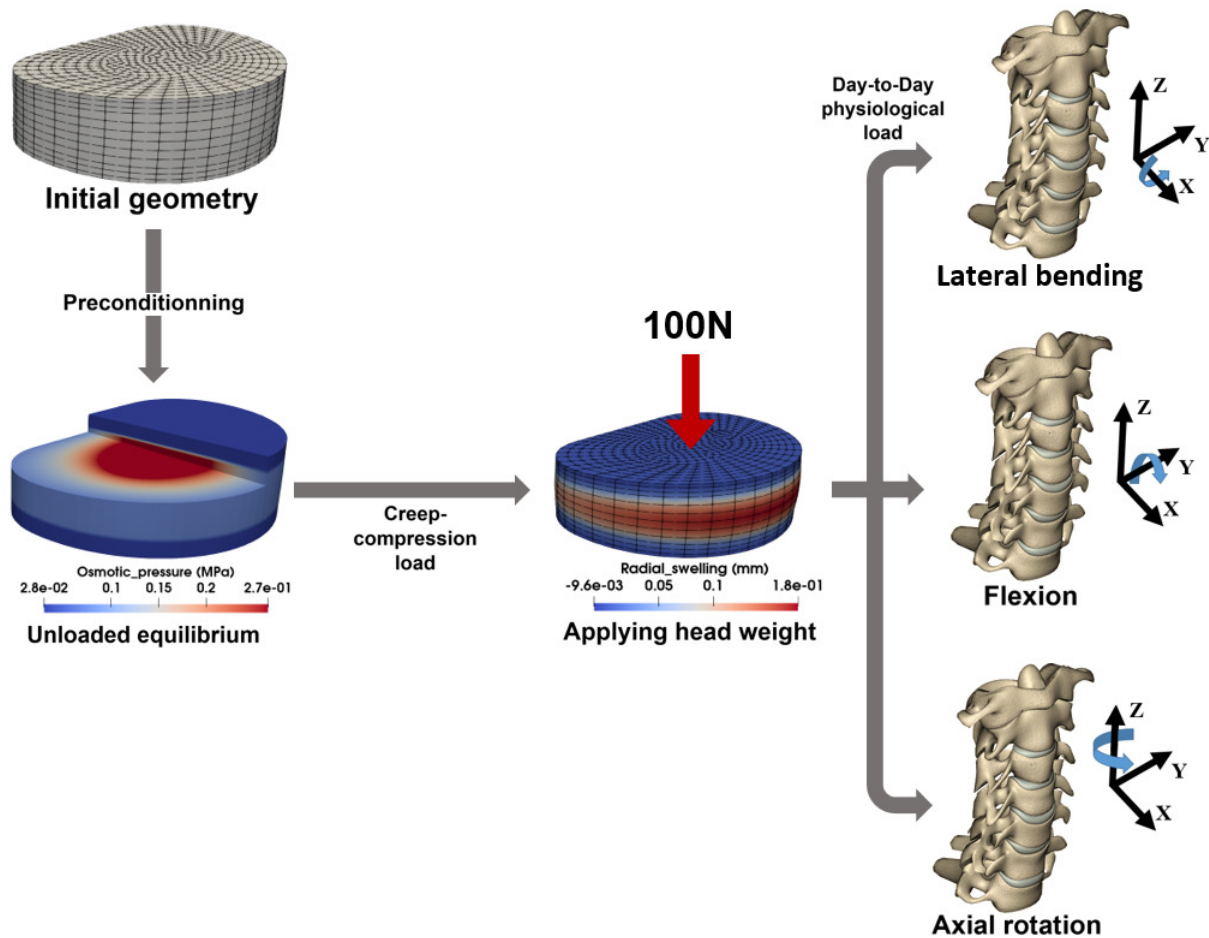


Figure 4: Representation of the IVD model simulation steps

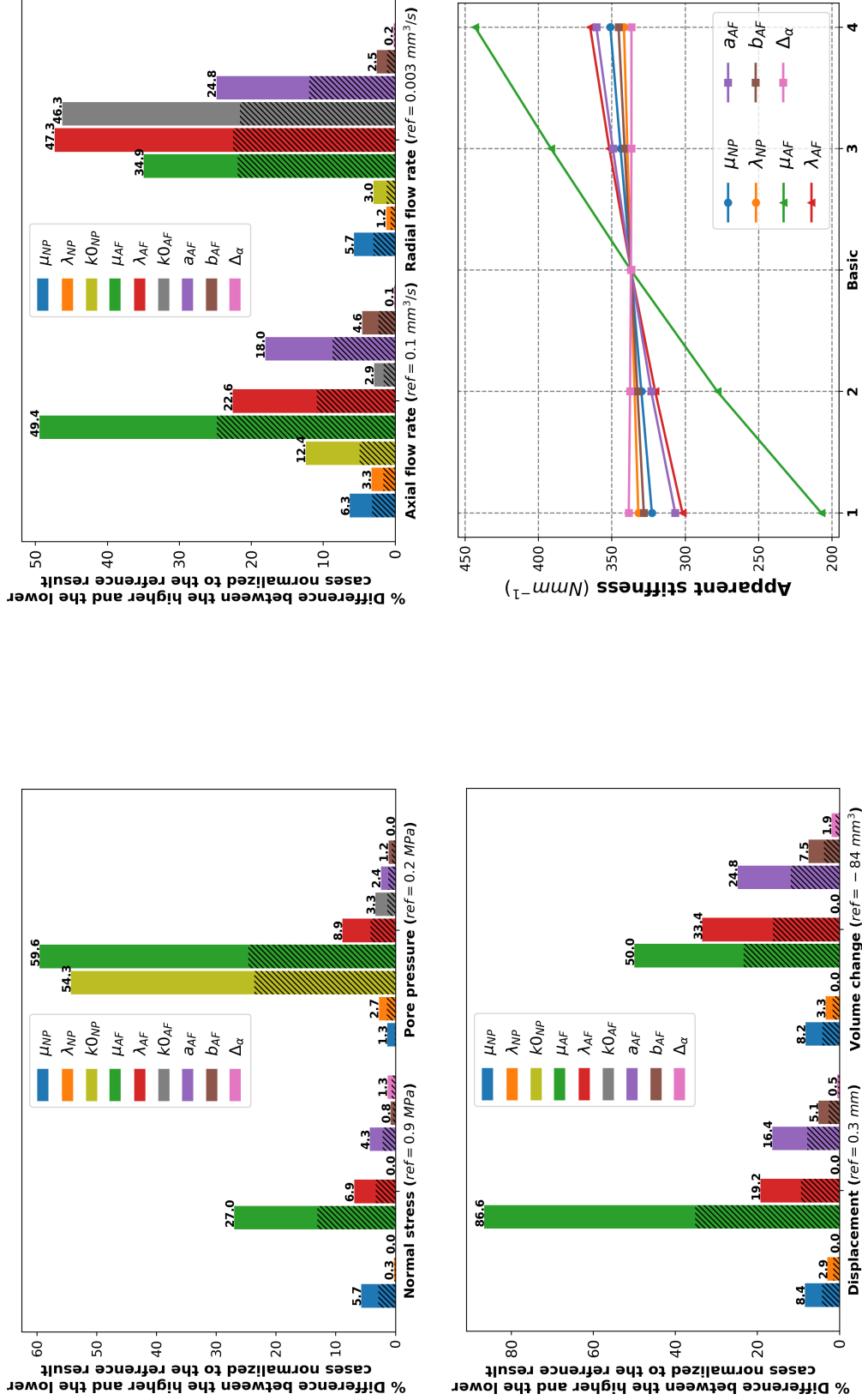


Figure 5: Impact of model parameters on IVD response to compression. The bar charts: difference between the 1 and the 4 cases (the 2 and 3 for the hatched area) normalized to the reference result (ref) obtained with the basic model parameters. The line graph corresponds to the evolution of the apparent stiffness in compression with the different scenarios of 7 parameters.

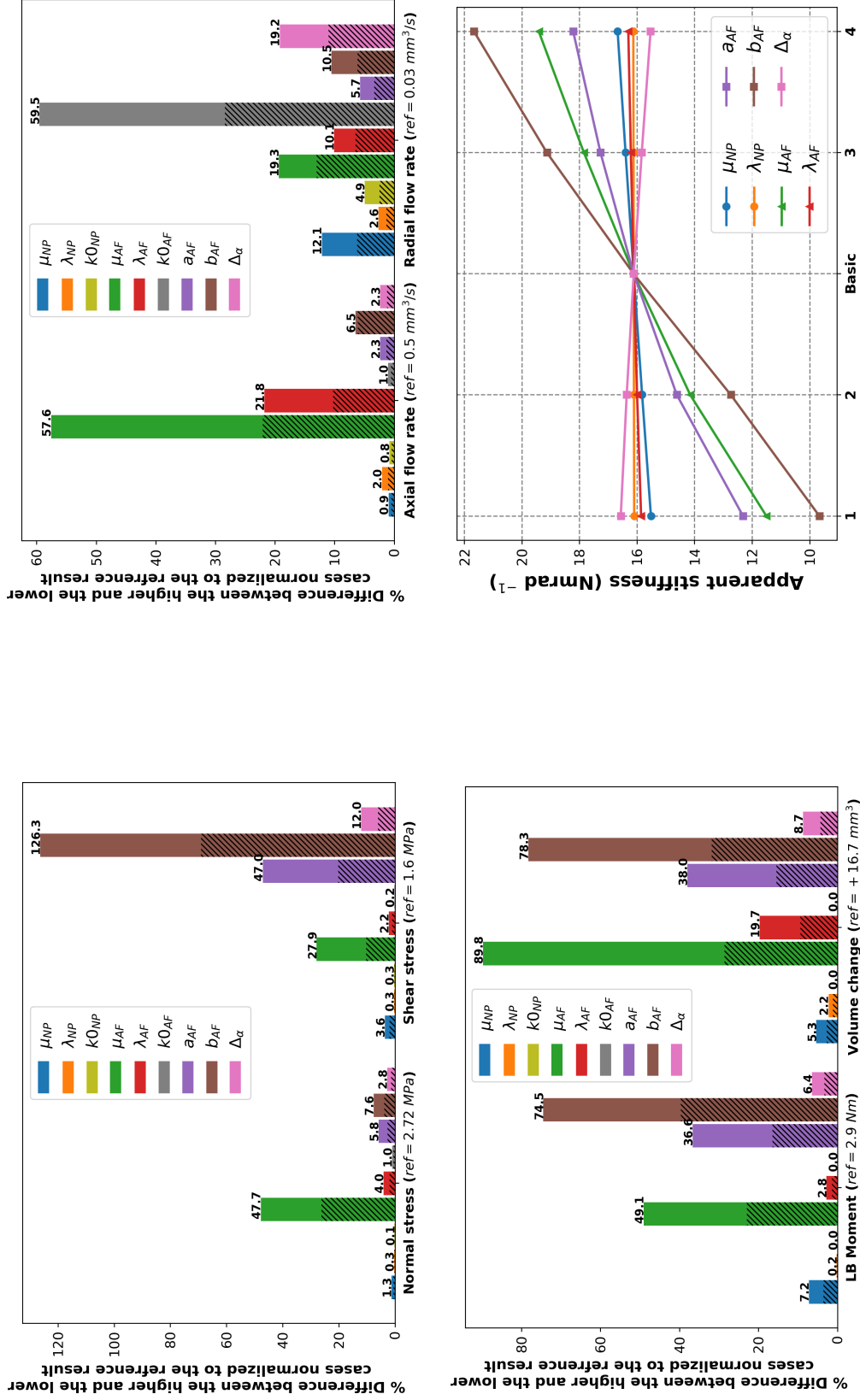


Figure 6: Impact of model parameters on IVD response to lateral bending. The bar charts: difference between the 1 and the 4 cases (the 2 and 3 for the hatched area) normalized to the reference result (ref) obtained with the basic model. The line graph corresponds to the evolution of the apparent stiffness in lateral bending with the different scenarios of 7 parameters.

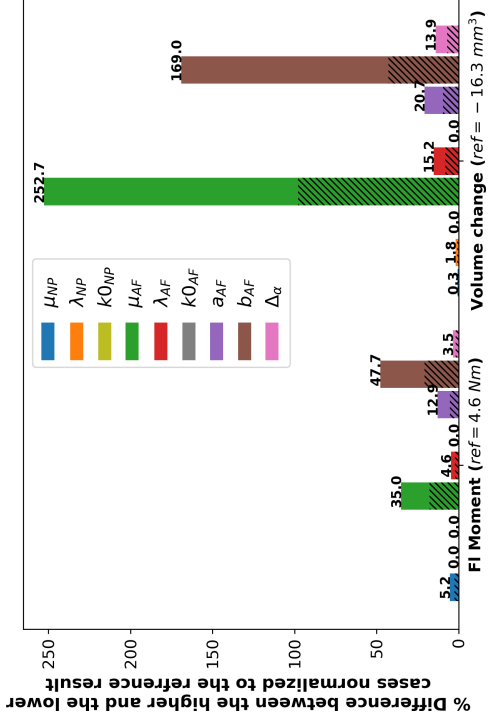
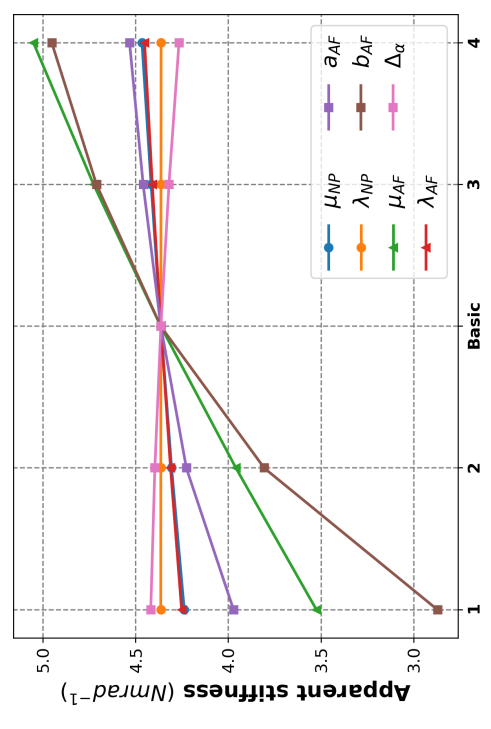
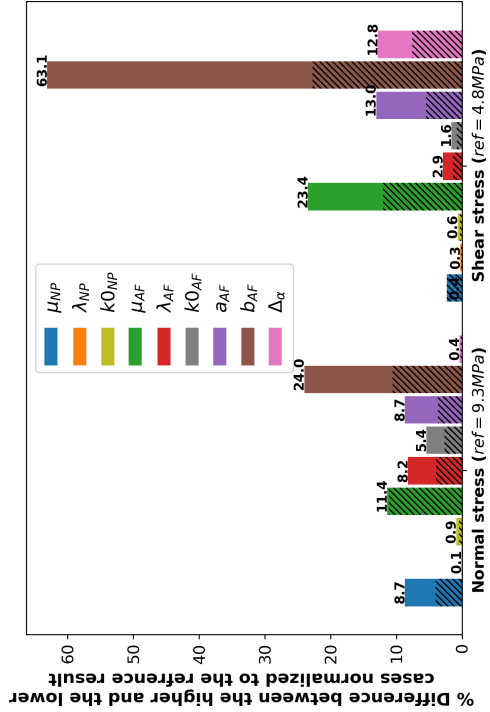
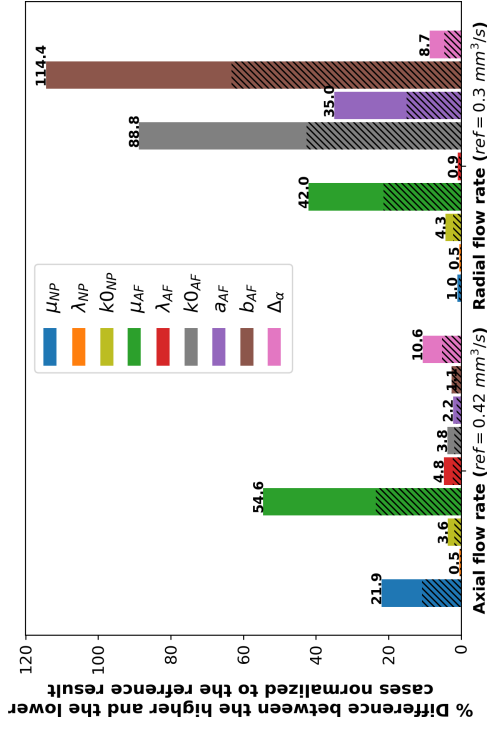


Figure 7: Impact of model parameters on IVD response to flexion. The bar charts: difference between the 1 and the 4 cases (the 2 and 3 for the hatched area) normalized to the reference result (ref) obtained with the basic model. The line graph corresponds to the evolution of the apparent stiffness in flexion with the different scenarios of 7 parameters.



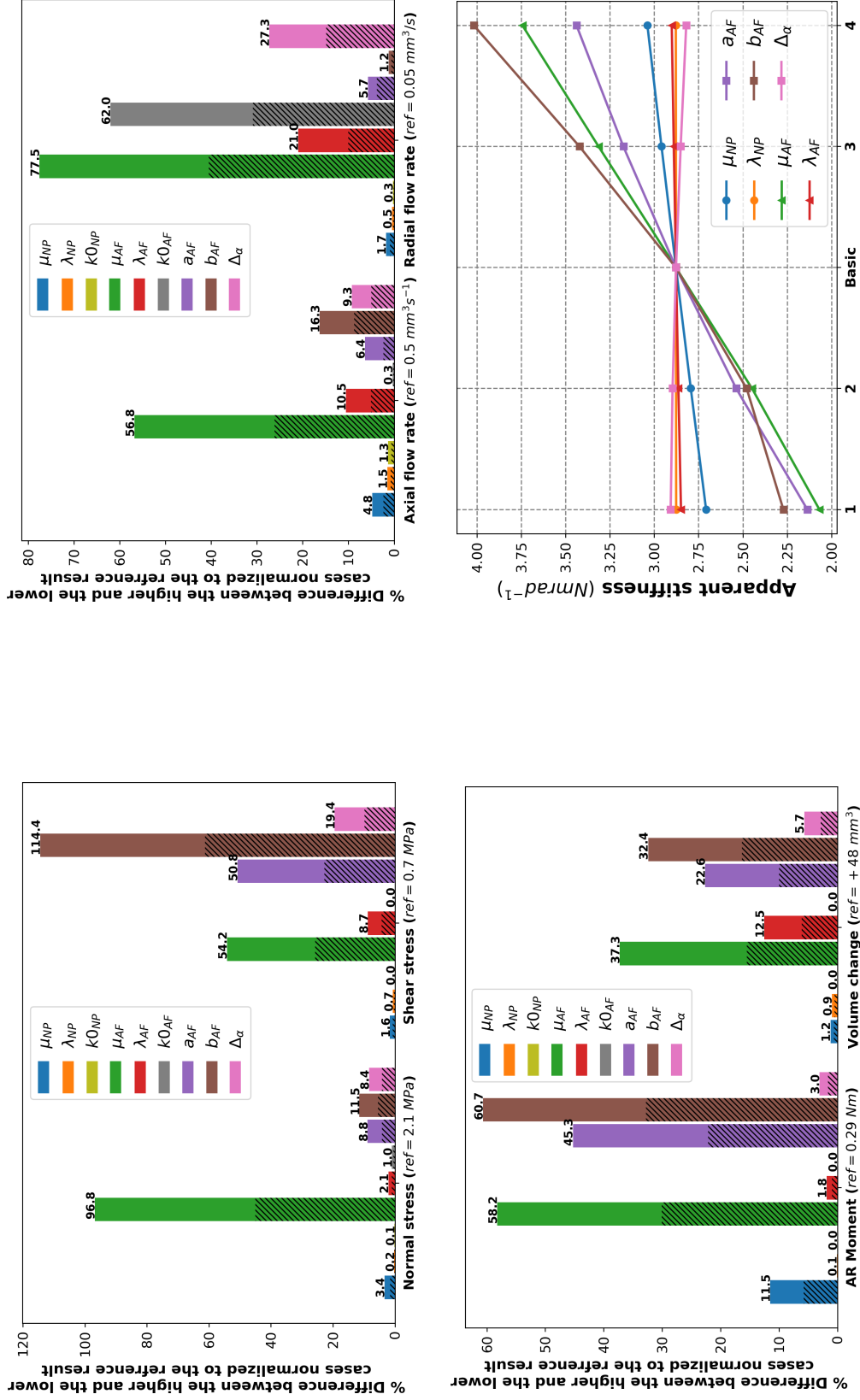


Figure 8: Impact of model parameters on IVD response to axial rotation. The bar charts: difference between the 1 and the 4 cases (the 2 and 3 for the hatched area) normalized to the reference result (ref) obtained with the basic model. The line graph corresponds to the evolution of the apparent stiffness in axial rotation with the different scenarios of 7 parameters.

Table 1: Applied intervertebral range of motion for the relaxation step for each load type. Motion: physiological motion of the whole cervical segment. Intervertebral rotation: C6-C7 rotation with *ILB*:lateral bending, *IFl*: flexion and *IAR*: axial rotation. Intervertebral translation: C6-C7 rotation with *P/A*: posterior(-)/interior(+), *L/R*: left (-)/Right(+) and *D/U*: down (-)/ up (+). For lateral bending and axial rotation, the intervertebral motion values correspond to 10° and 6°, respectively, of the C3-C7 segment and were taken from the curves in the cited reference. For the flexion, the intervertebral motion values correspond to the half of the studied range of motion (59.5° of the C1-T1 segment) in the cited reference.

Motion	Intervertebral rotation (°)			Intervertebral translation (mm)			Ref
	ILB (X)	IFl (Y)	IAR(Z)	P/A (X)	L/R (Y)	D/U (Z)	
Lateral bending	1.64	-0.15	-0.18	0.0	-0.34	0.08	[49]
Flexion	1.2	7.5	0.8	0.0	0.0	0.0	[51]
Axial rotation	1.1	-0.8	-0.3	0.1	-0.3	0.1	[49]

Table 2: Model parameters values for the basic model and the cases used for the parametric study. Variation of each parameter of this list was separately tested.

Parameter		Basic	Cases				References used in the definition of the intervals of study
			1	2	3	4	
<b>NP</b>	$\mu_{NP}$ (MPa)	0.4	0.1	0.25	0.55	0.7	[58, 53]
	$\lambda_{NP}$ (MPa)	0.3	0.1	0.2	0.4	0.5	[58, 53]
	$k0_{NP}^{\times 10^{-4}}$ (mm <sup>4</sup> /(Ns))	13	3	8	18	23	[52, 57]
	$C_{fc0}$ (mol/m <sup>3</sup> )	300	-				[58]
	$\phi_0$	0.8	-				[58]
<b>AF ground substance</b>	$\mu_{AF}$ (MPa)	1.2	0.4	0.8	1.6	2	[7, 57]
	$\lambda_{AF}$ (MPa)	1.3	0.2	0.75	1.85	2.4	[70, 4]
	$k0_{AF}^{\times 10^{-4}}$ (mm <sup>4</sup> /(Ns))	13	3	8	18	23	[52, 57]
	$C_{fc0}$ (mol/m <sup>3</sup> )	150	-				[11]
	$\phi_0$	0.7	-				[58]
<b>AF fibrillar network</b>	$a_{AF}$ (MPa)	1.2	0.3	0.75	1.65	2.1	[52, 54]
	$b_{AF}$	350	50	200	500	650	[11, 8]
	$\Delta\alpha$	5	0	2.5	7.5	10	[52, 71]
	$K_{AF}$	0.166	-				
<b>CEP</b>	$\mu_{CEP}$ (MPa)	7.14	-				[70]
	$\lambda_{CEP}$ (MPa)	10.44	-				[70]
	$k0_{CEP}^{\times 10^{-3}}$ (mm <sup>4</sup> /(Ns))	3.5	-				[70]
	$C_{fc0}$ (mol/m <sup>3</sup> )	90	-				[11]
	$\phi_0$	0.8	-				